Experimental evidence of lower hybrid wave scattering in Alcator C-Mod due to scrape off layer density fluctuations

E.H. Martin and C. Lau
Oak Ridge National Laboratory
Oak Ridge, TN, USA

G.M. Wallace, S. Shiraiwa, and R. T. Mumgaard
Massachusetts Institute of Technology, Plasma Science and Fusion Center
Cambridge, MA, USA

Abstract

Novel experimental measurements of the lower hybrid (LH) wave electric field vector, $\mathbf{E}_{LH}$, obtained in Alcator C-Mod using dynamic Stark spectroscopy are presented. Three key results were obtained by comparison with 3D full-wave COMSOL simulations using the cold plasma dielectric tensor and reflectometry-measured density profiles. ***(1)*** As a function of space and LH power, the magnitude of $\mathbf{E}_{LH}$ was found to agree with the full-wave simulation result. ***(2)*** The direction of $\mathbf{E}_{LH}$ was found to have a substantial poloidal component and is in strong disagreement with the nearly radial full-wave simulation result. ***(3)*** The addition of scrape off layer density fluctuations to the density profile implemented in the full-wave simulations can be used to explain the $\mathbf{E}_{LH}$ direction discrepancy. It is concluded that diffraction and scattering by turbulence-driven scrape off layer density fluctuations is the responsible mechanism behind the modification in the direction of $\mathbf{E}_{LH}$. These results further support the previously reported proposition that edge turbulence is an important mechanism behind the strong anomalous drop in LH current drive efficiency for diverted plasmas in the high-density regime.

1. INTRODUCTION

In high-density plasmas, lower hybrid current drive (LHCD) experiences a strong anomalous drop in efficiency as the density is increased [1-4] and was found to be inefficient in Alcator C-Mod for line-averaged densities approximately greater than 10^{20} m^{-3} [4]. Several mechanisms have been identified as parasitic to LHCD such as low-frequency scrape off layer (SOL) density fluctuations [5-14], parametric decay instability [15,16], collisional absorption [15,18], and pondermotive forces [19]. Recent experiments have determined that the edge region is responsible for the loss of current drive [20] and that turbulence plays a significant role [8,9,21]. These observations suggest that minimizing SOL density fluctuations is an important step toward efficient LHCD. However, the ordering of importance associated with the different phenomena has not been established. Detailed knowledge of the relative significance of each physical mechanism is necessary to develop appropriate launcher designs and mitigation techniques to address the drop in LHCD for high-density diverted plasmas.

To gain insight into the phenomena responsible for the anomalous drop in LHCD efficiency, the LH electric field vector ($\mathbf{E}_{LH}$) was directly measured in the edge region of Alcator C-Mod using dynamic Stark spectroscopy (DSS). Using a synthetic diagnostic, the experimental results were compared with 3D full-wave COMSOL simulations implementing the cold plasma dielectric tensor and reflectometry-measured density profiles. It was determined that the magnitude of $\mathbf{E}_{LH}$ agreed with the simulation. However, when comparing

the direction of $\mathbf{E}_{LH}$, a strong disagreement was observed. Experimentally, $\mathbf{E}_{LH}$ was found to be composed of nearly equal poloidal and radial components. In the simulation, $\mathbf{E}_{LH}$ was found to be nearly radial. Based on these results and previous experimental [5-9] and theoretical [10-12] work concluding that edge turbulence induces severe scattering of the LH wave in real and $k_\perp$ space, synthetic SOL density fluctuations were added to the simulation. This addition generated a substantial poloidal component in the $\mathbf{E}_{LH}$ vector and was able to reproduce the experimental results. It is therefore expected that diffraction and scattering by turbulence-driven SOL density fluctuations is the responsible mechanism behind the modification in the direction of $\mathbf{E}_{LH}$. This inference is significant because of the potentially severe effect these processes could have on LHCD as reported in previous work [8,9,21].

In this paper we do not specifically address how SOL density fluctuations affect LHCD. Instead, we provide direct experimental measurements of the LH wave electric field vector and correlate the results to SOL density fluctuations using full-wave modelling. The paper is organized as follows. In Sec. 2, the DSS diagnostic implemented on Alcator C-Mod and the spectral fitting process for $\mathbf{E}_{LH}$ is described. In Sec. 3, the details associated with the 3D full-wave COMSOL simulation, the SOL density fluctuation model, and the synthetic diagnostic for $\mathbf{E}_{LH}$ are presented. In Sec. 4, the experimental results are described, highlighting key behaviors in both the magnitude and direction of $\mathbf{E}_{LH}$. In Sec. 5, the conclusions are outlined linking edge turbulence to diffraction and scattering of the LH wave.

2. DYNAMIC STARK SPECTROSCOPY

The one-electron atom has a quantum structure that is highly sensitive to the electric field. This structure can be directly probed through a measurement of the spectral line profile. The result is a powerful diagnostic for electric fields in the fusion device, especially when laser-based spectroscopic techniques are implemented [22,23].

For a time periodic electric field having an angular frequency, ω, much larger than the transition probability, A_{ki}, the perturbation to the quantum structure is dictated by the dynamic Stark effect [24]. This phenomenon is fundamentally different from the static Stark effect when viewed from a classical standpoint. For the static electric field, the spectral line profile is split into a series of components based on the magnitude of the electric field. For a time periodic electric field having $\omega >> A_{ki}$, the effect on the spectral line profile is substantially different. In this case, the spectral line profile experiences a series of satellites evenly spaced about the line center. The spacing is determined by the electric field frequency (not the magnitude) and occurs at integer multiples of ω. The physical picture describing the dynamic Stark effect is that of a multiphoton process in which the photon associated with the electronic transition absorbs or emits photons associated with the time periodic electric field. The evenly spaced satellite structure is due to the addition (absorption) or subtraction (emission) of photon energy. For high-frequency electric fields (>10's GHz), the satellite structure is easily observed in the spectra [25,26]. In the <10 GHz frequency range, the satellite structure is too closely spaced and individual satellites cannot be observed using passive optical emission spectroscopy. The frequency of the LH wave in Alcator C-Mod is 4.6 GHz; therefore, individual satellites are not observed. Instead, the combined effect of multiple satellites results in global alteration of the spectrum. The time periodic electric field vector is determined by fitting the Schrodinger equation to the shape of the spectral line profile.

2.1. Diagnostic implementation on Alcator C-Mod

Polarized passive optical emission spectroscopy was implemented on Alcator C-Mod to measure two orthogonally polarized D_β spectra. The β-Balmer series transition (n=4 to 2) was selected from an optimization between optical emission signal-to-noise ratio and electric field sensitivity. For a *pure* electric (E) or magnetic (B) field, the orthogonally polarized spectra are referred to as π (parallel to E or B-field) and σ (perpendicular to E or B-field). Decomposing the unpolarized spectrum into its polarized components can be extremely beneficial because the field affects the π and σ polarized spectra differently. If these spectra are measured and fit to the Schrodinger equation simultaneously, an additional constraint is provided, allowing the field to be determined with greater accuracy. A nomenclature with respect to the magnetic field is adopted here because the Zeeman effect is significant stronger than the dynamic Stark effect.

The experimental setup consists of two periscopes connected fiber optically to a f=500 mm Acton spectrometer having a 2400 line/mm grating. The scientific camera used to acquire the spectral data was a Princeton Instruments ProEM CCD and was programmed to integrate optical emission over a 50 ms window. The periscopes consist of a polarizing beam splitter and two lenses focusing the π and σ polarized emission into separate fiber optics. Four spectra were acquired every 50 ms: π and σ polarization at two measurement locations. Fig. 1 presents a top-down cross section of Alcator C-mod indicating the position of the periscopes and the sightline geometry used to observe the polarized D_β spectra.

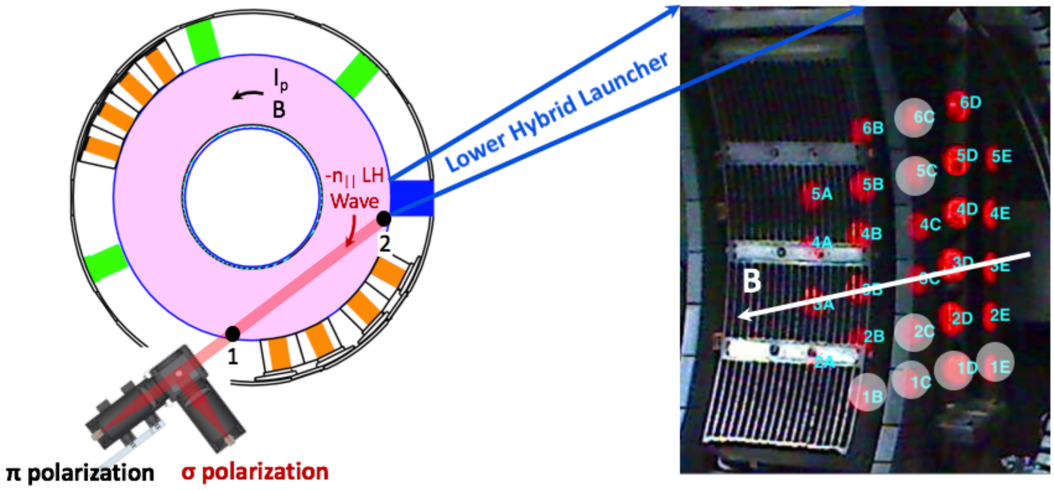

Figure 1. Top-down cross section of Alcator C-Mod indicating the location of the two periscopes used to observe the π and σ polarized D_β spectra (periscope dimensions not to scale). The 27 magnetic field–aligned measurement locations are shown as red circles in the image of the LH launcher. The measurement locations of the data presented in this paper are highlighted in white.

The periscopes were aligned such that the polarizing beam splitter's axis was 14 degrees clockwise from vertical. This resulted in nearly parallel and perpendicular polarization with respect to the equilibrium magnetic field. Optical emission was observed in two regions within a sightline, labelled as 1 and 2 in Fig. 1, due to the large ionization fraction in the core. The diameter of the sightline at region 1 is 12 mm and at region 2 is 35 mm. A diverging sightline was designed to maximize the collection volume in region 2, where $\mathbf{E}_{LH}$ is being measured. The mounting bracket for the periscopes was designed to allow access to 27

predetermined magnetic field–aligned views of the LH launcher. The periscopes were backlit to determine the exact measurement location. A composite image of the LH launcher showing the 27 available measurement locations as red circles is present in Fig. 1. The white highlighted locations are associated with data presented in this paper. Given that only two measurement locations could be observed simultaneously, multiple repeated discharges were necessary to obtain the full $\mathbf{E}_{LH}$ data set.

2.2. Spectra fitting for extraction of $\mathbf{E}_{LH}$

The spectral line profile is calculated using the Explicit Zeeman Stark Spectral Simulator (EZSSS). This code solves the time-dependent Schrodinger equation non-perturbatively for the electron's quantum structure considering a static magnetic field vector and time periodic electric field vector. The spectral line profile is then calculated using first-order time-dependent perturbation theory, the electric dipole connection operator, and the sightline geometry in which optical emission is observed. References [24,27,28] contain further details and a complete derivation. It is important to note that both the electric and magnetic field vectors must be considered simultaneously in the Schrodinger equation due to nonlinear coupling. To determine $\mathbf{E}_{LH}$, the π and σ polarized D_β spectra were fit simultaneously using the spectralFIT (sFIT) code. A global optimization routine is implemented in sFIT to minimize the mean square error between the experimental and theoretical spectrum. EZSSS is used in sFIT for the theoretical calculations.

The model used to fit the spectral data consists of three components: two outboard (regions 1 and 2 of Fig. 1) and one inboard. The latter was found to be necessary due to reflections from the surface terminating the sightline. The spectra associated with the outboard components are calculated using the equilibrium magnetic field determined from EFIT (4.1 T), sightline geometry, polarizing beam splitter angle, neutral temperature (0.8 eV), and density determined from edge Thompson scattering (5×10^{19} m^{-3}). The neutral temperature and density are required to calculate the Doppler and Stark broadening, respectively. Additionally, for region 2, the $\mathbf{E}_{LH}$ vector is included. The region of origin associated with the inboard emission is unknown. Therefore, a zero LH power spectrum was recorded for each discharge and fit with $\mathbf{E}_{LH}$=0 to determine the parameters (intensity, magnetic field, Doppler shift, etc.) representing the inboard component spectrum. The intensity of the inboard component was typically 10% of the total spectrum. The outboard D_β radial intensity profile was calculated using a 1D kinetics neutral transport code, KN1D [29] and was found to peak near the last closed flux surface. Integrating over the sightline volume, it was determined that the intensity ratio of region 2 to region 1 is 1.8. The three components of $\mathbf{E}_{LH}$ are the only fit variables for spectra obtained when the LH launcher was powered. The components of $\mathbf{E}_{LH}$ are chosen to be aligned perpendicular ($E_{LH,\perp 1}$ and $E_{LH,\perp 2}$) and parallel ($E_{LH,||}$) to the equilibrium magnetic field vector.

To illustrate the diagnostics sensitivity to $\mathbf{E}_{LH}$, Fig. 2 presents simulated π (left) and σ (right) polarized spectral line profiles as a function of electric field magnitude for $\mathbf{E}_{LH}=E_{LH,\perp 1}$ (a), $\mathbf{E}_{LH}=E_{LH,\perp 2}$ (b) and $\mathbf{E}_{LH}=E_{LH,||}$ (c). The simulations were conducted with EZSSS using the model described above for measurement location 1D (see Fig. 1). The difference between the profiles of the π and σ polarized spectra is predominately due to the magnetic field. Ideally, the σ polarized spectrum experiences strong Zeeman splitting while the π polarized spectrum experiences no Zeeman splitting. However, the polarization axis associated with the experimental setup is not exactly aligned parallel to the magnetic field due to the sightline geometry. A small amount of Zeeman splitting is present in the π profile. The asymmetry observed in the spectra is due to reflections from the inboard side.

A generalization of the approximate global behavior of the spectral line profile can be made by comparing the simulations presented in Fig. 2. The profiles are found to either broaden (beginning to split) or narrow (becoming center peaked) as the magnitude of $\mathbf{E}_{LH}$ is increased. The specific behavior depends on both the direction of $\mathbf{E}_{LH}$ and the spectral polarization. However, for all $\mathbf{E}_{LH}$ directions the π and σ polarized spectral line profiles experience opposite trends. The black dashed arrows in Fig. 2 indicated the profile trends as the $\mathbf{E}_{LH}$ magnitude is increased.

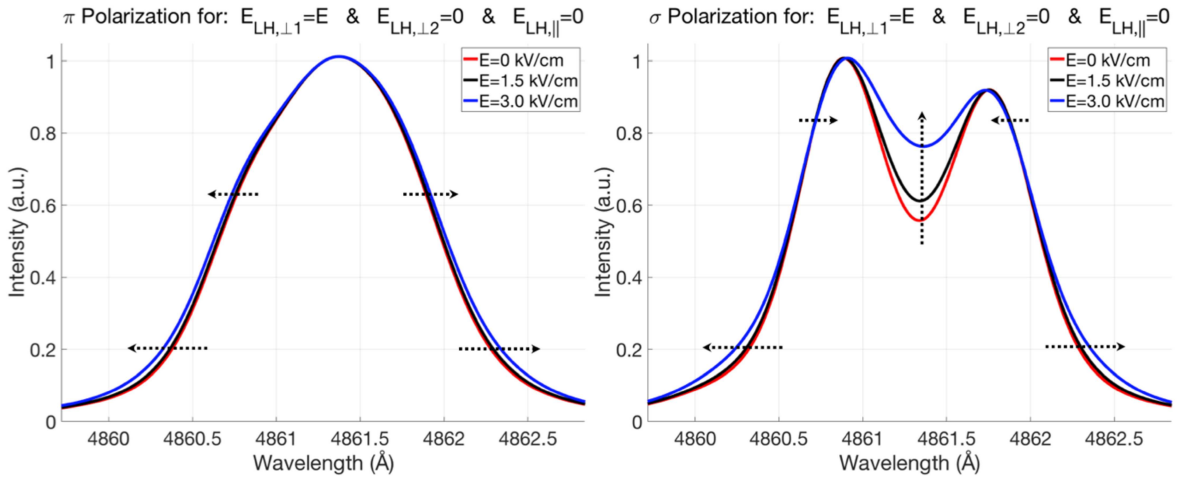

(a)

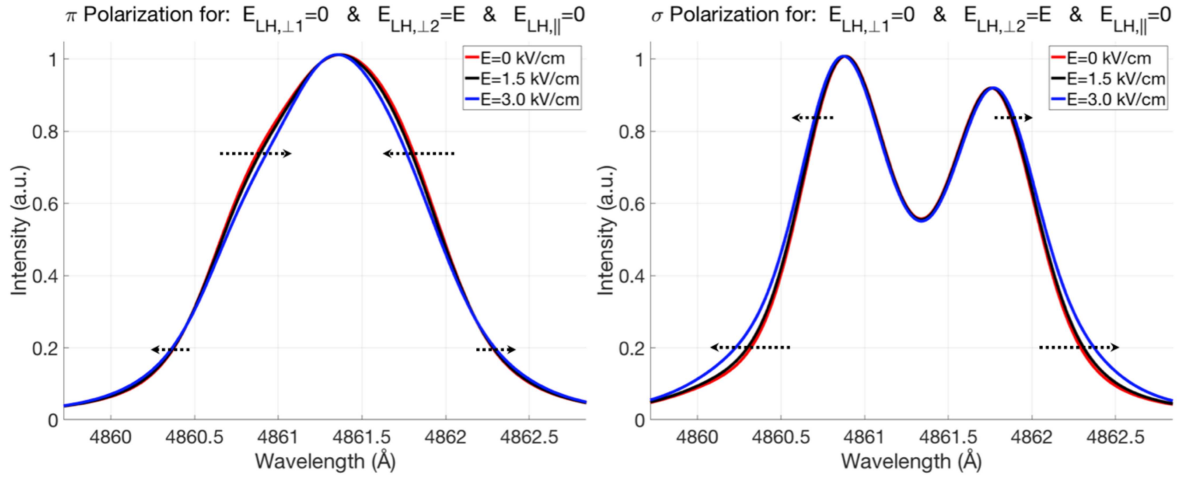

(b)

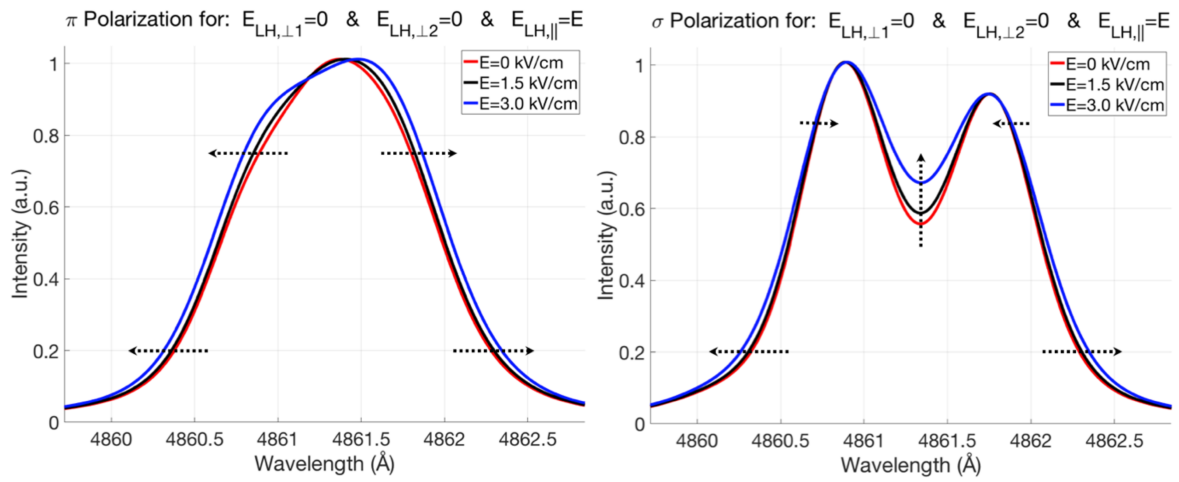

(c)

Figure 2. EZSSS simulated π (left) and σ (right) polarized D_β spectral line profiles as a function of $\mathbf{E}_{LH}$ magnitude for a directions $\mathbf{E}_{LH}$=$E_{LH,\perp 1}$ (a), $\mathbf{E}_{LH}$=$E_{LH,\perp 2}$ (b) and $\mathbf{E}_{LH}$=$E_{LH,||}$ (c).

Similar behavior is observed for the $\mathbf{E}_{LH}$=$E_{LH,\perp 1}$ (Fig. 2a) and $\mathbf{E}_{LH}$=$E_{LH,||}$ (Fig. 2c) directions: the π profile broadens and the σ profile becomes increasingly center peaked. For the $\mathbf{E}_{LH}$=$E_{LH,\perp 2}$ (Fig. 2b) direction: the π profile becomes increasingly center peaked and the σ profile broadens. Opposite trends are observed for the $\mathbf{E}_{LH}$=$E_{LH,\perp 1}$/$\mathbf{E}_{LH}$=$E_{LH,||}$ and $\mathbf{E}_{LH}$=$E_{LH,\perp 2}$ directions. Understanding the global behavior of the polarized profile's is important for qualitative and diagnostic feasibility purposes. However, to extract $\mathbf{E}_{LH}$ accurately a quantitative analysis is required and entails systematic fitting of the Schrodinger equation to the experimental spectra. The latter is conducted using EZSSS and sFIT, as described above. Measuring both π and σ profiles simultaneously has the tremendous benefit of increasing the fit model known to unknown ratio from 1/3 to 2/3 (two spectra / three $\mathbf{E}_{LH}$ components) ~ a factor of two. Additionally, systematic errors due to broadening mechanisms such as Doppler or Stark can be eliminated because both the π and σ profiles have identical responses. This provides a critical fitting constraint and is required to exact $\mathbf{E}_{LH}$ having a magnitude ≤ 3 kV/cm using the spectroscopy setup described here.

Figure 3 depicts experimental (left) and simulated (right) data for the π (a) and σ (b) polarized D_β spectral line profiles. The measurement location was 1D. In each figure, three spectra are presented and correspond to 0, 213, and 378 kW of net LH power. The simulated data was generated with EZSSS using the model described above.

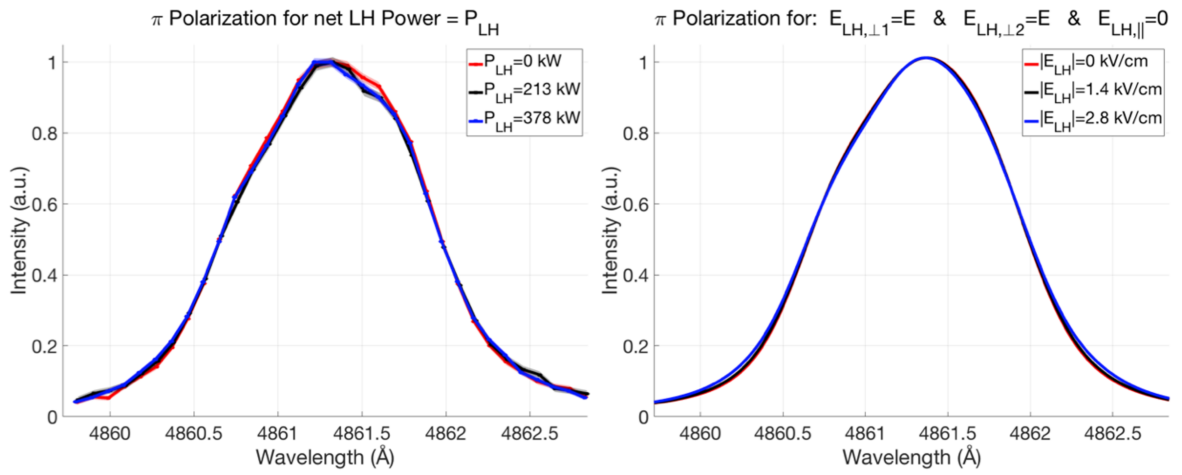

(a)

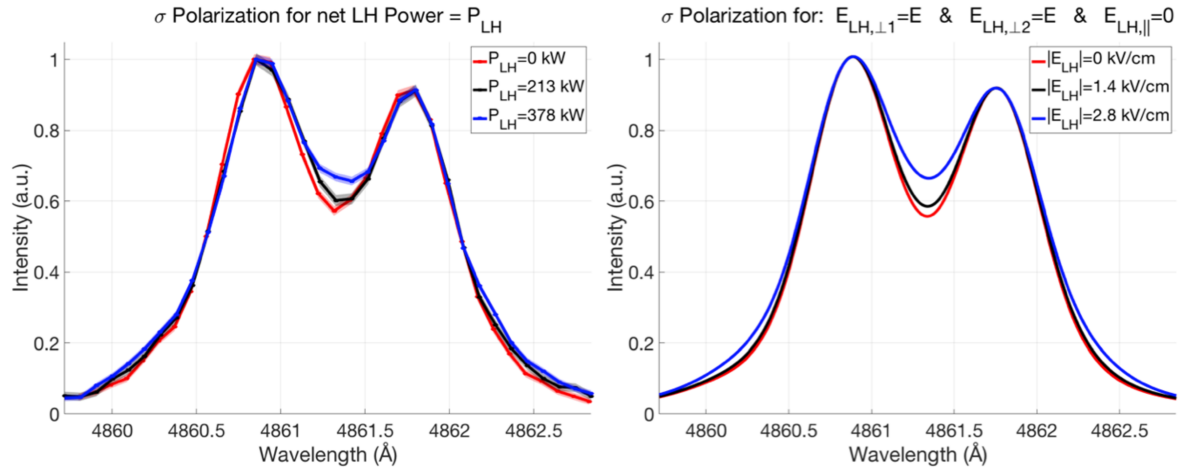

(b)

Figure 3. Experimental (left) and simulated (right) π (a) and σ (b) polarized D_β spectral line profiles as a function LH power. The measurement location was 1D (see Fig. 1).

The electric field vector associated with the simulations was determined by fitting the experimental π and σ profiles simultaneously with sFIT. The signal-to-noise ratio of the experimental measured spectra is ≤ 2 percent and is represented by the highlighted region. Comparing the spectra presented in Fig. 3 it is observed that as the net LH power is increased the π profile narrows near the peak and broadens at the base, however this affect is minimal. The σ profile experiences broadening at the base and becomes increasingly center peaked. This behavior can only be observed if $\mathbf{E}_{LH}$ is perpendicular to the equilibrium magnetic field vector because a parallel component would cause significant broadening of the π profile. The minimal response of the π profile while σ profile becomes increasingly center peaked can only be explained by nearly equal $E_{LH,\perp 1}$ and $E_{LH,\perp 2}$ components. This is due to an effective cancelation of the broadening and narrowing in the π profile caused by the $E_{LH,\perp 1}$ and $E_{LH,\perp 2}$ components, respectively (see Figs. 2a and 2b). The response of the experimentally measured π and σ profiles is emulated by the simulations (right) presented in Fig. 3 when $E_{LH,\perp 1}=E_{LH,\perp 2}$ and $E_{LH,||}=0$.

In order to increase the accuracy of $\mathbf{E}_{LH}$, the π and σ polarized D_β spectra were fit a total of eight times using different wavelength windows with sFIT. The reported $\mathbf{E}_{LH}$ vector is the average. Fig. 4 presents spectral fits for four of the eight wavelength windows. The markers

are associated with the experimental spectra and the solid lines with the fit. The net LH power was 378 kW and the location of the measurement was 1D. The fit determined values of the $\mathbf{E}_{LH}$ components are listed in Fig. 4.

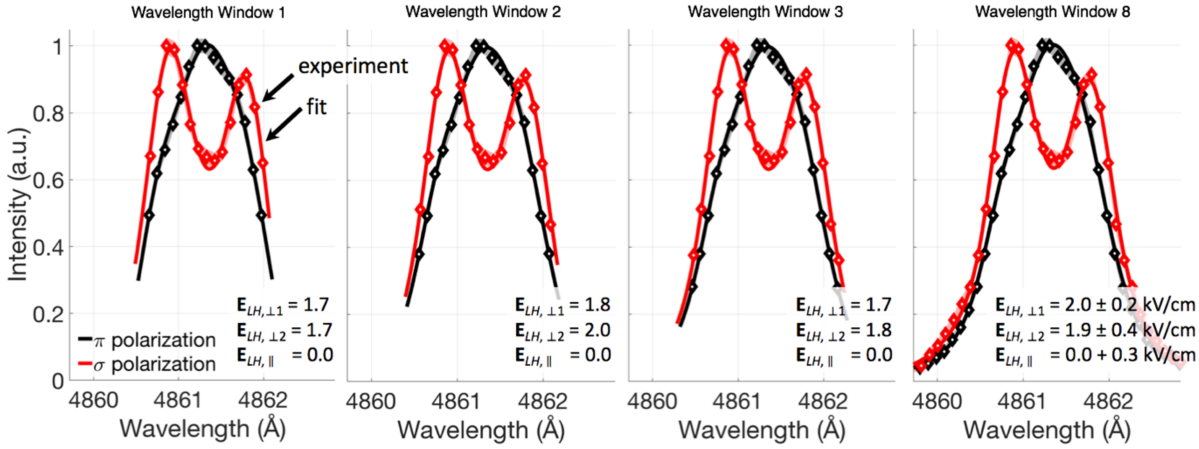

Figure 4. Experimental (markers) and fit (line) π and σ polarized D_β spectral line profiles associated with measurement location 1D for a launched LH power of 378 kW. The reported $\mathbf{E}_{LH}$ vector is the average obtained from the eight wavelength window fits.

sFIT implements a global minimization routine by completely discretizing the model variable space and calculating the reduced χ statistical parameter at each discretization point. The reduced χ is calculated independently for the π and σ profiles and summed together, $\chi=\chi_\pi+\chi_\sigma$. The values of the model variables at the minimum reduced χ are selected and a subsection of the model variable space about this point is further discretized. The reduced χ in this subsection is calculated and the minimum is again selected. The model variables at this discretization point are taken as the best fit values. This process is continued until convergence, typically three iterations. The model variable space consists of the three components of $\mathbf{E}_{LH}$: $E_{LH,\perp1}$, $E_{LH,\perp2}$ and $E_{LH,||}$. The value of $E_{LH,||}$ was predominantly found to be zero and never exceeded the noise floor of 0.3 kV/cm. This is the expected result due to the outward radial bound of the measurement volume. Figure 5 presents the reduced χ as a function of the model variable space for $E_{LH,||}$=0 kV/cm associated with the fit presented in Fig. 4 for wavelength window 8.

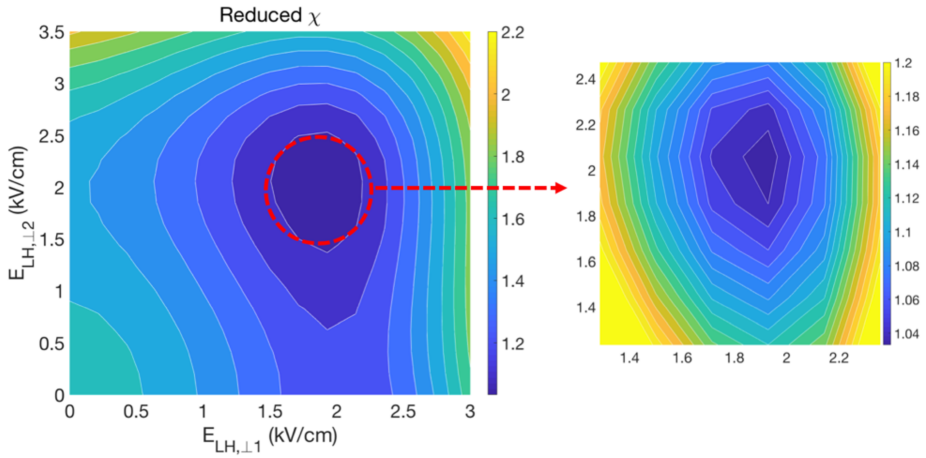

Figure 5. The reduced χ statistical parameter as a function of the model variable space for $E_{LH,||}$=0 kV/cm. The measurement location was 1D and the net LH power was 378 kW. The

experimental and fit π and σ polarized D_β spectral line profiles are associated with wavelength window 8 of Fig. 4.

The error in $\mathbf{E}_{LH}$ was calculated using a Monte Carlo approach. Spectra were simulated using the model implemented to fit the experimental data. Twenty sets of noise, based on random and Poisson statistics, were generated. The random noise was set to yield a signal-to-noise ratio of 5 percent (2.5x the actual signal-to-noise ratio) to generate a conservative estimate of the error. A unique set of noise was added to the simulated π and σ profiles, and a fit was carried out. The standard deviation with respect to the simulated value was calculated and assigned as the error. The $E_{LH,\perp 1}$ and $E_{LH,\perp 2}$ components of the $\mathbf{E}_{LH}$ were varied from 0 to 2.5 kV/cm and $E_{LH,||}$ was set to zero. Figure 6 depicts the error associated with the fit determined perpendicular components of $\mathbf{E}_{LH}$ as a function of their magnitude.

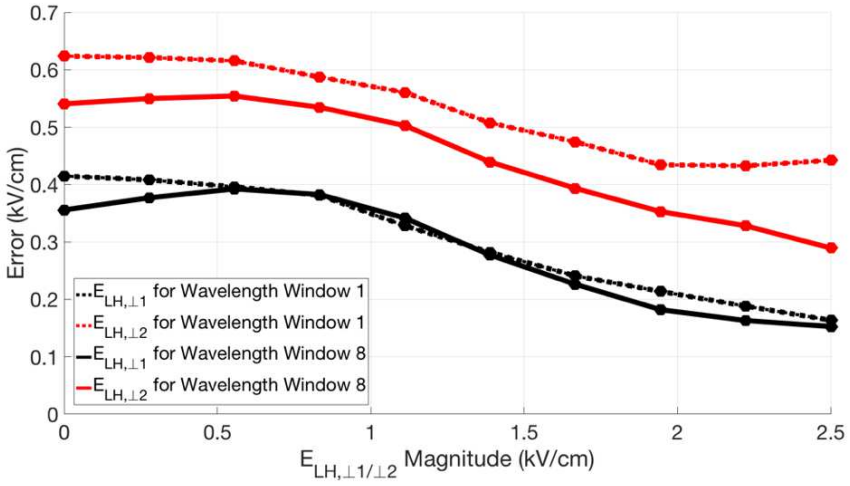

Figure 6. The error associated with the fit determined perpendicular components of $\mathbf{E}_{LH}$ as a function of their magnitude. A Monte Carlo approach was implemented using a conservative signal-to-noise ratio of 5 percent. The actual experimental signal-to-noise ratio was ≤ 2 percent. The extreme wavelength windows (see Fig. 4) are presented and yield similar results. The smallest (1) and largest (8) wavelength windows (see Fig. 4) are presented. The error associated with the $E_{LH,\perp 2}$ component is approximately 1.5x that of the $E_{LH,\perp 1}$ and is due to the $E_{LH,\perp 2}$ having a weaker effect on the σ profile (see Figs. 2a and 2b).

3. 3D FULL WAVE MODELING OF THE LOWER HYBRID WAVE

To interpret the DSS $\mathbf{E}_{LH}$ measurements, it is necessary to develop a synthetic diagnostic. This has been achieved using a 3D full wave cold-plasma finite element model within COMSOL Multiphysics.

3.1. Simulation model

LH waves have been modelled previously using 2D and 3D full-wave simulations [30-33]. The simulation model presented in this paper adapts similar techniques by solving the vector wave equation in 2D axisymmetric geometry using COMSOL Multiphysics. This is done for an arbitrary but fixed toroidal mode number. The extension to 3D is achieved by summing over many toroidal mode numbers determined from the toroidal spectrum specified by the LH launcher. A full 3D model is very memory intensive and not achievable with the

available computational resources. The 2D axisymmetric vector wave equation is given by Eq. (1), and the Fourier sum of toroidal modes is given by Eq. (2):

$$\nabla \times \left[\nabla \times \mathbf{E}_{LH,m}(r,z)\right] - \frac{\omega^2}{c^2}\left[\overleftrightarrow{\boldsymbol{\varepsilon}} \cdot \mathbf{E}_{LH,m}(r,z)\right] = 0 \tag{1}$$

$$\mathbf{E}_{LH}^{3D}(r,z,\varphi) = \sum_m A_m \mathbf{E}_{LH,m}(r,z) e^{im\varphi} \tag{2}$$

where ω is the LH wave angular frequency, m is the toroidal mode number, $\overleftrightarrow{\boldsymbol{\varepsilon}}$ is the cold plasma dielectric tensor, c is the speed of light, A_m is the amplitude of the m^{th} toroidal mode, $\mathbf{E}_{LH,m}$ is the 2D LH electric field vector associated with the m^{th} toroidal mode, and $\mathbf{E}_{LH}^{3D}$ is the 3D LH electric field vector. The radial density profile was measured by SOL reflectometry [34] and edge Thomson scattering [35] and is assumed to be constant on a magnetic flux surface. Radial and poloidal magnetic field profiles were provided by EFIT. The density and magnetic field are necessary inputs for the cold plasma dielectric tensor. Collisions have been included through an effective imaginary component in the electron mass [34]. A spatially constant collision frequency was assumed for this simulation. The collision frequency was found to have an insignificant effect on the direction of $\mathbf{E}_{LH}^{3D}$ and a small effect on the magnitude of $\mathbf{E}_{LH}^{3D}$ in the region of interest. The LH launcher dimensions and 90° input phasing of its 16 columns is used to determine A_m. A full description of this model can be found in Ref. [37].

Figure 7 presents the 3D full wave simulation of the magnitude of $\mathbf{E}_{LH}^{3D}$ for a net LH power of 330 kW and a line-averaged density of 1.3×10^{20} m^{-3}. A composite image of the LH launcher showing the 27 measurement locations as red circles is superimposed. The white highlighted locations are associated with data presented in this paper. Four resonance cones are clearly visible and correspond to the four rows of the LH launcher. To gauge the error associated with the simulation, a sensitivity study of $\mathbf{E}_{LH}^{3D}$ on the density profile and measurement location was conducted. It was found that the $\mathbf{E}_{LH}^{3D}$ direction was impervious to these parameters (~3% change) while the magnitude experienced a significant alteration (~50% change). The simulation accuracy has important implications for the interpretation of the results presented in Sec. 4.

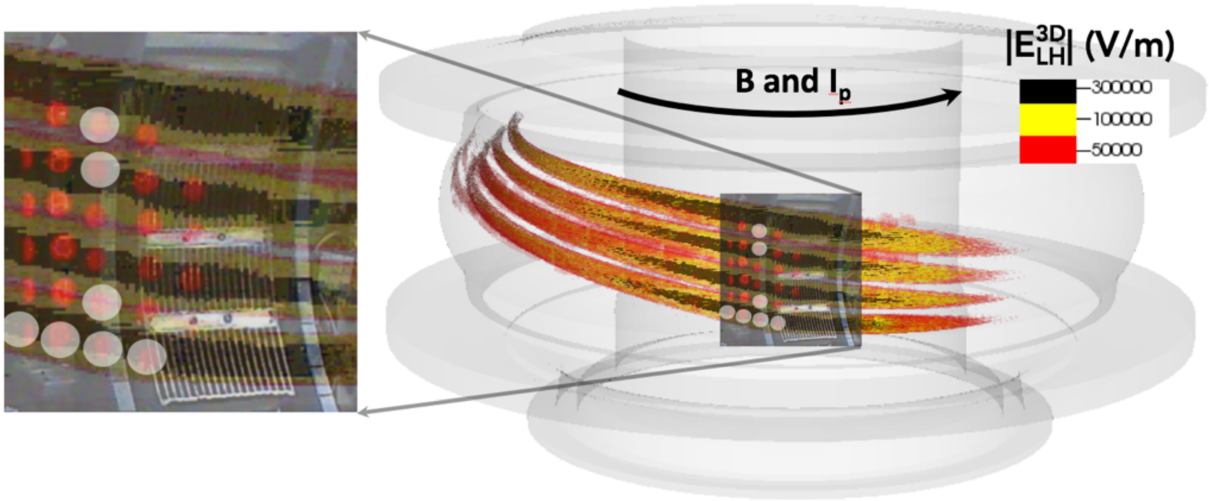

Figure 7. 3D full-wave COMSOL simulation of the magnitude of $\mathbf{E}_{LH}^{3D}$ for a LH net power of 330 kW and a line-averaged density of 1.3 × 10^{20} m^{-3}. An image of the LH launcher showing the magnetic field–aligned measurement locations as red circles is superimposed. The measurement locations of the data presented in this paper are highlighted in white.

3.2. Scrape off layer density fluctuation model

The simulation model presented in Sec. 3.1 assumes the radial density profile is constant on a magnetic flux surface. Previous experimental work presents strong evidence that the LH wave is scattered in both real and $k_\perp$ space by SOL density fluctuations [5-9]. Furthermore, theoretical predictions within Ref. [10] predict significant $k_\perp$ scattering for typical tokomak parameters. Based on these findings, a synthetic turbulence model was formulated. The functional form is given by Eq. (3):

$$n_e = n_{eo}\left[(1 + \tilde{n}/n\, e^{-\frac{(r-r_c)^2}{r_w}} \sin\left(\frac{2\pi p}{\lambda}\right) e^{-\frac{(p-p_c)^2}{p_w^2}}\right] \quad (3)$$

where n_{eo} is the reflectometry-measured radial density profile, λ is the poloidal wavelength of the fluctuations, and $\tilde{n}/n$ is the fractional density fluctuation amplitude. The parameters controlling the density fluctuation poloidal location and width and radial location and width are: p_c, p_w, r_c, and r_w, respectively. The values of these locations and width parameters are chosen such that the density fluctuations occur in the near SOL and peak at the midplane. This behavior was prescribed based on experimental turbulence measurements [38-40] and a BOUT simulation of a similar Alcator C-Mod discharge [41]. This simplified model was solely designed to provide an estimate on the effect of turbulent-driven SOL density fluctuations on $\mathbf{E}_{LH}$. Further details can be found in Ref. [37].

It was found that the inclusion of synthetic turbulence over a range of λ, spanning 0.5 to 20 mm, and $\tilde{n}/n$, spanning 0.15 to 0.95, significantly altered both the magnitude and direction of $\mathbf{E}_{LH}^{3D}$. Additionally, the propagation of the LH wave was substantially modified and complete reflection in the far SOL was observed in some cases. The range of λ and $\tilde{n}/n$ is based on previous experimental turbulence measurements in Alcator C-Mod [38-40]. Figure 8 presents the magnitude of $\mathbf{E}_{LH,m}$ for the dominant toroidal mode incorporating synthetic turbulence into the simulation having λ=5 mm and $\tilde{n}/n$ varied from 0 to 0.9.

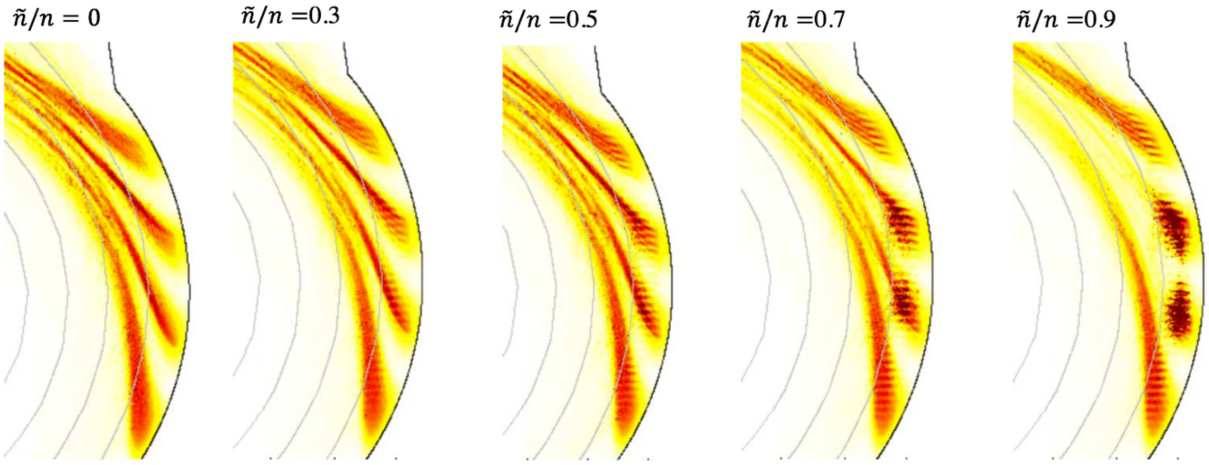

Figure 8. 2D full-wave COMSOL simulation of the magnitude of $\mathbf{E}_{LH,m}$ for the dominant toroidal mode, m=-180. The synthetic turbulence model described by Eq. (3) was incorporated with λ=5 mm and $\tilde{n}/n$ varied from 0 to 0.9.

3.3. Synthetic diagnostic for $\mathbf{E}_{LH}$

The DSS diagnostic implements a passive spectroscopic technique to acquire D_β spectra, resulting in an integrated measurement over the sightline volume. In order to directly compare the 3D full wave simulation result ($\mathbf{E}_{LH}^{3D}$) with the experimentally determined LH wave electric field vector ($\mathbf{E}_{LH}$), a weighted volumetric average over the sightline is calculated. The radial intensity profile, $I_{D\beta}$, of the D_β optical emission is used as the weighting function. This quantity is calculated from KN1D using the radial plasma density and temperature profiles measured from reflectometry and Thomson scattering, neutral pressure from an ionization gauge, and wall geometry. The synthetic diagnostic of $\mathbf{E}_{LH}$ is calculated using Eq. (4).

$$\boldsymbol{E}_{LH} = \frac{\int |\mathrm{E}_{LH,\parallel}^{3D}| I_{D\beta} dV}{\int I_{D\beta} dV} \hat{\parallel} + \frac{\int |\mathrm{E}_{LH,\perp 1}^{3D}| I_{D\beta} dV}{\int I_{D\beta} dV} \hat{\perp}_1 + \frac{\int |\mathrm{E}_{LH,\perp 2}^{3D}| I_{D\beta} dV}{\int I_{D\beta} dV} \hat{\perp}_2 \quad (4)$$

The magnitude of each component is taken because the DSS diagnostic is incapable of detecting the relative phase angle between the components given the resolution of our spectroscopic system is used to measure the spectra.

4. RESULTS

The target plasma was an H-mode discharge having a line-averaged density of 1.3×10^{20} m^{-3}. The equilibrium magnetic field was 5.4 T, and the plasma current was 0.8 MA. These conditions were selected because no LHCD was observed [4]. The LH power was ramped stepwise up to 400 kW. The timing was synchronized such that the LH power was held constant during the acquisition of spectral data, occurring every 50 ms. Results obtained at seven spatial locations in front of the LH launcher are presented. The measurement locations are highlighted white in Figs. 1 and 7 and correspond to a vertically aligned column (1C, 2C, 5C, and 6C) and a magnetic field–aligned row (1B, 1C, 1D, and 1E). These sets of data will be referred to as the "vertical" and "horizontal" locations, respectively. The coordinate system used to reference the location of the vertically and horizontally grouped measurements has its origin at the center of the LH launcher.

4.1. Magnitude of $\mathbf{E}_{LH}$

The simulated magnitude of $\mathbf{E}_{LH}$ was found to be very sensitive to the radial density profile, measurement location, and SOL density fluctuations. These sensitives resulted in a larger error associated with the simulation (~50%) when compared with the experiment (~30%). To yield an accurate insight into the global behavior of the LH wave in the edge plasma, the average over space and LH power is presented in this paper. The average was performed on $\mathbf{E}_{LH}$ determined, as a function of space and LH power, from each π and σ polarized spectra set. Fig. 9 presents the magnitude of $\mathbf{E}_{LH}$ spatially averaged over the vertical (a) and horizontal (b) measurement locations as a function of LH power. Excellent agreement with the full-wave simulation result was found, and the expected theoretical scaling, proportional to the square root of LH power, is observed for both vertical and horizontal location averages. The black dashed line is a fit to the experimental data. This trend is

identical to the DSS results obtained in Tore Supra for an *L*-mode discharge having a high fraction of plasma current being sustained by LHCD [28].

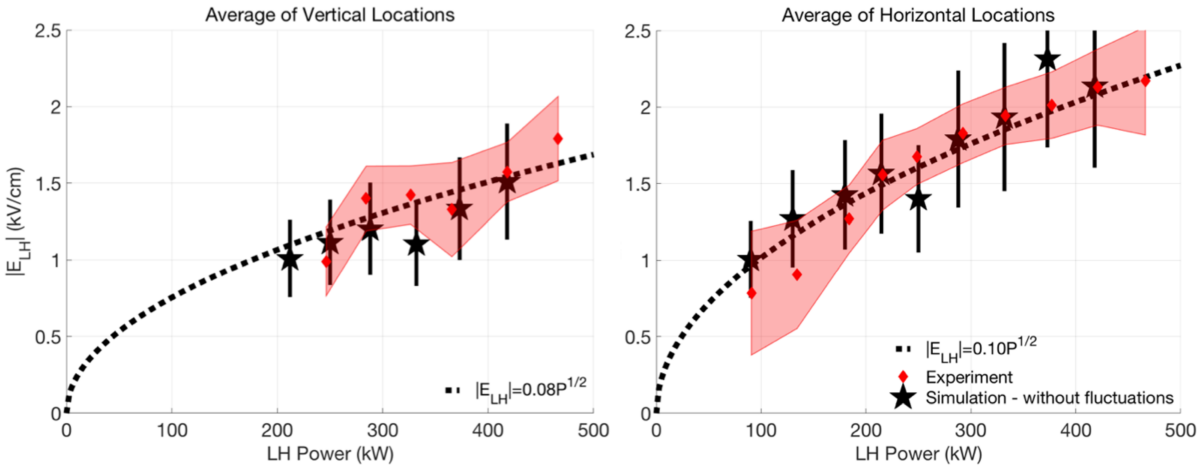

(a) (b)

Figure 9. Magnitude of $\mathbf{E}_{LH}$ averaged over the white highlighted vertical (a) and horizontal (b) locations of Fig. 1 as a function of LH power. The experimental data was found to scale with the square root of the LH power. The black dashed line is a fit to the experimental data.

These results indicate that the LH wave power is fully present in the $-n_{\parallel}$ component of the wave as imposed by the launcher waveguide array phasing and that no impediment with respect to power is observed.

To provide insight into the LH resonance cone structure and absorption by the edge plasma near the launcher, the magnitude of $\mathbf{E}_{LH}$ as a function of space was investigated by performing an average over LH power. Figure 10 presents the magnitude of $\mathbf{E}_{LH}$ averaged from 200 to 400 kW of LH power as a function of vertical (a) and horizontal (b) measurement location. The simulation was conducted with and without SOL density fluctuations. Based on previous turbulence measurements in Alcator C-mod [38-40], the parameters of the synthetic turbulence model were set to λ=5 mm and $\tilde{n}/n$=0.75. Agreement within uncertainties was found between the experimental and simulation data without SOL density fluctuations. With the addition of synthetic turbulence, similar results are produced. However, two of the seven measurement locations (1B and 1C) experience a strong increase in their simulated value, leading to a substantial disagreement. This is believed to be driven by the static nature of the synthetic turbulence model and the strong localization of the LH resonance cones. Additionally, the synthetic turbulence model significantly increased the simulations sensitivity to the collisionality and was found to produce an artificially high $\mathbf{E}_{LH}$ magnitude.

Detailed spatial structure of the LH resonance cones is not accessible due to the measurement volume being on the order of the waveguide dimensions. However, the nearly constant response of the vertical measurements of the magnitude of $\mathbf{E}_{LH}$ presented in Fig. 10a suggests that the resonance cones are being broadened spatially. This observation supports a conclusion described in previous theoretical [12] and experimental work which measured a significant loss of resonance cone structure in the core attributed to low-frequency density fluctuations [5-7]. The horizontal measurements of the magnitude of $\mathbf{E}_{LH}$ presented in Fig. 10b indicate that LH wave is propagating along the magnetic field line without strong absorption near the launcher. Absorption would produce elevated magnitudes of $\mathbf{E}_{LH}$

followed by a strong decay in its value along the magnetic field line. This behavior is observed in the simulation with SOL density fluctuations and is caused by an artificial sensitivity to the collisionality.

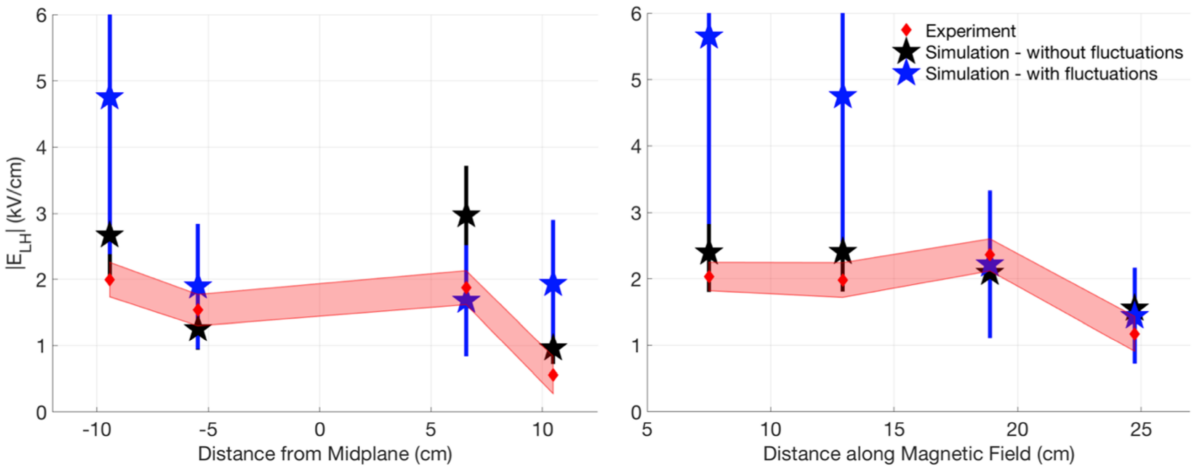

(a) (b)

Figure 10. Magnitude of $\mathbf{E}_{LH}$ averaged over LH power as a function of the white highlighted vertical (a) and horizontal (b) locations of Fig. 1. The coordinate system origin is located at the LH launcher center.

4.2. Direction of $\mathbf{E}_{LH}$

Unlike the magnitude of $\mathbf{E}_{LH}$, the direction was found to be insensitive to the radial density profile and measurement location. Only SOL density fluctuations were observed to significantly affect its value. This resulted in a simulation error (~3%) much smaller than the experimental error (~30%). It was found in both the experimental and simulated $\mathbf{E}_{LH}$ that the parallel component was much smaller than the perpendicular components. Thus, the direction of $\mathbf{E}_{LH}$ is presented as the inverse tangent of the perpendicular component's ratio. At the midplane, the poloidal and radial directions correspond to 0 and 90 degrees, respectively. Figure 11 presents the direction of $\mathbf{E}_{LH}$ averaged from 200 to 400 kW of LH power as a function of distance from the midplane for the vertical and horizontal sets of measurements. The black dashed line indicates the absolute value of the angle between the surface normal vector associated with the last closed flux surface and the horizontal direction. The error bars associated with the simulated data are present in Fig. 11, however, they are concealed by the marker size due to its small amplitude, approximately 3 percent.

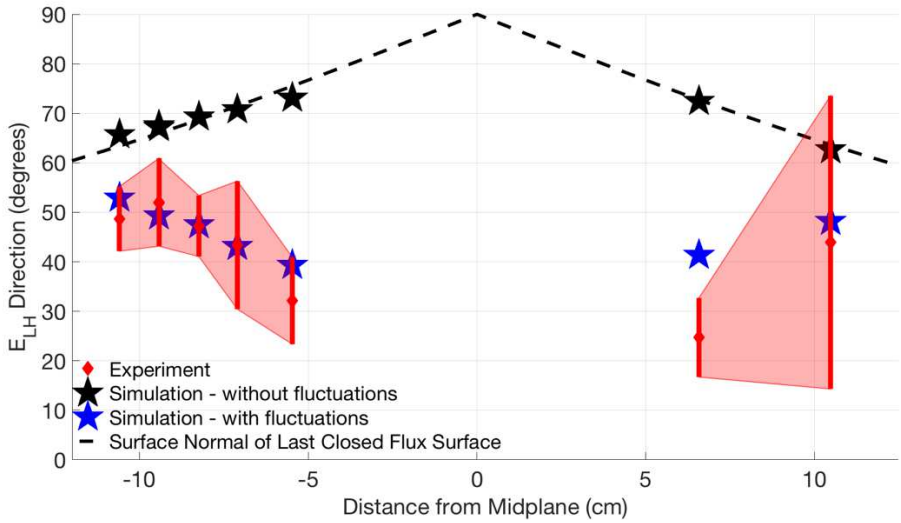

Figure 11. Direction of $\mathbf{E}_{LH}$ averaged over LH power as a function of distance from the midplane for the white highlighted vertical and horizontal locations of Fig. 1. The direction of $\mathbf{E}_{LH}$ is only dependent on the distance from the midplane, remaining constant along the magnetic field. This result is constant with the highly anisotropic characteristic scale lengths of turbulent fluctuations perpendicular and parallel to the equilibrium magnetic field vector.

It was found experimentally that $\mathbf{E}_{LH}$ contained a poloidal component having a magnitude on the order or greater than that of the radial component. The poloidal component was found to be a strong function of poloidal angle, increasing towards the midplane, and a weak function of toroidal angle, remaining approximately constant. The constant toroidal angle functionality was determined by subtracting out the poloidal angle dependence, determined from the vertical set of measurements, from the response measured along the magnetic field, determined from the horizontal set of measurements. This result strongly disagrees with the nearly radial direction simulated without SOL density fluctuations. Including the synthetic turbulence model having λ=5 mm and $\tilde{n}/n$=0.75 resulted in a significant alteration in the direction $\mathbf{E}_{LH}$ such that agreement within uncertainties was achieved. This result is consistent with previous theoretical [10-12] and experimental observations hypothesizing [5-7] and correlating [8,9] LH wave scattering with SOL density fluctuations.

A parametric study of λ and $\tilde{n}/n$ was conducted to determine the applicability of our synthetic turbulence model. Figure 12 presents the direction of $\mathbf{E}_{LH}$ as a function of λ and $\tilde{n}/n$ simulated at measurement location 1C. It was determined that a wide range of values could be used to obtain results similar to those presented in Fig. 11. This finding is significant because the LH wave will experience the instantaneous SOL density fluctuation profile due to its propagation speed being much greater than the fluctuation frequency. In other words, in the frame of the LH wave the density fluctuations are static. Using gas puff imaging, a wide range of λ (5 to 10 mm) and $\tilde{n}/n$ (exceeding 1) values have been experimentally measured in Alcator C-mod [40]. Thus, the alteration in the direction of the LH wave due to SOL density fluctuations will be an average over this range and will yield similar results to that presented in Fig. 11.

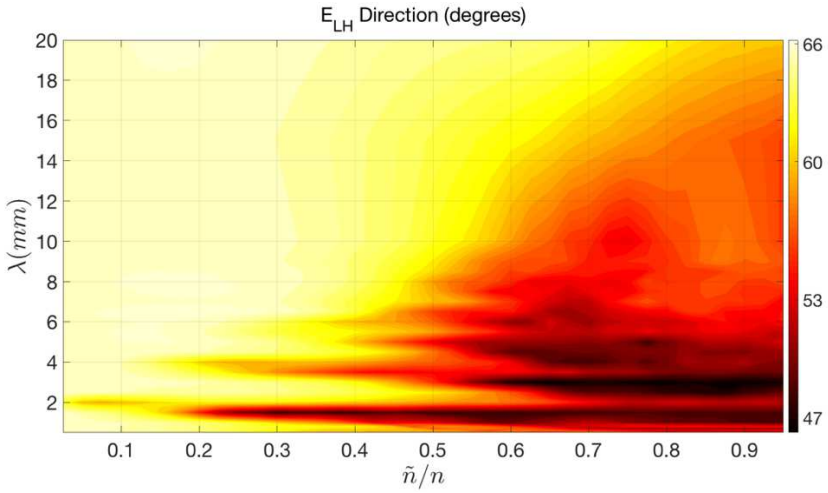

Figure 12. Simulated direction of $\mathbf{E}_{LH}$ including SOL density fluctuations as a function of λ and $\tilde{n}/n$ at measurement location 1C.

5. CONCLUSIONS

The LH wave power is proportional to the square of its electric field vector. Therefore, the DSS-measured magnitude of $\mathbf{E}_{LH}$ provides insight into the behavior of the LH wave power in the SOL near the launcher. Two conclusions are drawn. First, when spatially averaged, the LH wave power is following the theoretically predicted scaling with respect to launched power. Second, when averaged over launched power, the spatial distribution of LH wave power is in agreement with the 3D full-wave simulations. These conclusions indicate that the full LH wave power is present in the $-n_{\parallel}$ component of the wave and that strong absorption near the launcher structure is not occurring. A significantly different result was found for the direction of $\mathbf{E}_{LH}$. When SOL density fluctuations are not included, the simulation predicts a nearly radial direction. Experimentally, a poloidal component on the order or greater than that of the radial component was observed. The poloidal component was found to be a strong function of poloidal angle, increasing toward the midplane, and a weak function of toroidal angle, remaining approximately constant. This result is in strong disagreement with the simulation and even trends oppositely with respect to the distance from the midplane. Including midplane-peaked synthetic turbulence, the simulation was able to predict the behavior of the experimentally determined $\mathbf{E}_{LH}$ direction within uncertainties. Furthermore, a range of λ and $\tilde{n}/n$ values consistent with gas puff imaging observations obtained in Alcator C-Mod [40] produce the same effect. This result is important because from the LH wave's frame of reference the SOL density fluctuations can be considered static. On the millisecond time scale, the $\mathbf{E}_{LH}$ direction will be determined by an average over a range of instantaneous λ and $\tilde{n}/n$ values (or spectrum of values) and will yield similar results to those obtained for λ=5 mm and $\tilde{n}/n$=0.75.

In conclusion, we present direct experimental measurements of $\mathbf{E}_{LH}$ indicating that absorption of LH wave power near the launcher is not significant and that strong scattering in $k_{\perp}$ space attributed to SOL density fluctuations is occurring. The scattering was found to consistently increase toward the midplane independent of the measurement location. Applying a synthetic turbulence model to the full wave simulations suggests that scattering is driven by midplane peaking SOL density fluctuations in the range of λ=5 mm and $\tilde{n}/n$=0.75. The SOL density fluctuations required to reproduce the experimental observations are fully consistent with turbulence measurements in Alcator C-Mod [38-40]. These results further

support the conclusions from previous experimental [5-9] and theoretical [10-12] work linking SOL density fluctuations with LH wave scattering in $k_\perp$ space. Specifically, Refs. [9,10,21] are particularly important because SOL density fluctuations have been correlated to the anomalous drop in LHCD efficiency. Reactor-relevant scenarios are likely to experience enhanced turbulence in the SOL, further motivating the need to test innovative solutions such as the high field side launch lower hybrid scheme [42-44].

ACKNOWLEDGMENTS

The authors would like to thank P. Bonoli for his guidance and M. Umansky for suppling the BOUT simulation results of Ref. [41]. This work was supported under US Department of Energy contract nos. DE-AC05-00OR22725 and DE-FC02-99ER54512. Alcator C-Mod is a DOE Office of Science User Facility. This manuscript has been authored by UT-Battelle, LLC, under contract DE-AC05-00OR22725 with the US Department of Energy (DOE). The US government retains and the publisher, by accepting the article for publication, acknowledges that the US government retains a nonexclusive, paid-up, irrevocable, worldwide license to publish or reproduce the published form of this manuscript, or allow others to do so, for US government purposes. DOE will provide public access to these results of federally sponsored research in accordance with the DOE Public Access Plan (http://energy.gov/downloads/doe-public-access-plan).

REFERENCES

[1] Cesario R., et al., Current drive at plasma densities required for thermonuclear reactors, Nat. Commun. **1** (2010) 55.
[2] Goniche M., et al., Lower hybrid current drive at high density on Tore Supra, Nucl. Fusion **53** (2013) 033010.
[3] Ding B.J., et al., Experimental investigations of LHW-plasma coupling and current drive related to achieving H-mode plasmas in EAST, **53** (2013) 113027.
[4] Wallace G.M., et al., Absorption of lower hybrid waves in the scrape off layer of a diverted tokamak, Phys. Plasmas **17** (2010) 082508.
[5] Surko C.M., et al., Study of driven lower-hybrid waves in the Alcator tokamak using CO_2-laser scattering **43** (1979) 1016.
[6] Slusher R.E., et al., Study of driven lower-hybrid waves in the Alcator A tokamak using CO_2 laser scattering, Phys. Fluids **25** (1982) 457.
[7] Watterson R.L., et al., Spectrum and propagation of lower-hybrid waves in a tokamak plasma, Phys. Fluids **28** (1985) 2622.
[8] Ridolfini Pericoli V. et al., Lower hybrid current drive efficiency in tokamaks and wave scattering by density fluctuations at the plasma edge, Nucl. Fusion **51** (2011) 113023.
[9] Ridolfini Pericoli V. et al., Frequency spectral broadening of lower hybrid waves in tokamak plasmas-causes and effects, Nucl. Fusion **32** (1994) 469.
[10] Bellan P.M. et al., Effect of density fluctuations on lower hybrid resonance cone propagation, Phys. Fluids **21** (1978) 592.
[11] Andrews P.L. et al., Spectral broadening of lower-hybrid waves by time-dependent fluctuations, Phys. Fluids **26** (1983) 2546.
[12] Edward O., Lower hybrid wave scattering by density fluctuations, Phys. Fluids **22** (1979) 1732.
[13] Bonoli P. et al., Toroidal and scattering effects on lower-hybrid wave propagation, Phys. Fluids **25** (1982) 359.

[14] Madi M., et al., Propagation of the lower hybrid wave in a density fluctuating scape-off layer (SOL), Plasma Phys. Control. Fusion **57** (2015) 125001.
[15] Baek S.G., et al., Measurements of ion cyclotron parametric decay of lower hybrid waves at the high-field side of Alcator C-Mod, Plasma Phys. Control. Fusion **55** (2013) 052001.
[16] Li M.H., et al., Study on lower hybrid current drive efficiency at high density towards long-pulse regimes in Experimental Advanced Superconducting Tokamak, Phys. Plasma **21** (2014) 062510.
[17] Wallace G.M., et al., Lower hybrid current drive at high density in Alcator C-Mod, Nucl. Fusion **51** (2011) 083032.
[18] Shiraiwa S., et al., Progress towards steady-state regimes in Alcator C-Mod, Nucl. Fusion **53** (2013) 113028.
[19] Preynas M., et al., Experimental characterization and modelling of non-linear coupling of lower hybrid current drive power on Tore Supra, Nucl. Fusion **53** (2013) 013012.
[20] Faust I.C., et al., Lower hybrid wave edge power loss quantification on the Alcator C-Mod tokamak, Phys. Plasmas **23** (2016) 056115.
[21] Baek S.G., et al., Observation of efficient lower hybrid current drive at high density in diverted plasmas on the Alcator C-Mod tokamak, Phys. Rev. Lett. **121** (2018) 055001.
[22] Martin E.H., et al., Applications of Doppler-free saturation spectroscopy for edge physics studies, Rev. Sci. Instrum. **87** (2016) 11E402.
[23] Reymond L., et al., Using Laser-Induced Rydberg Spectroscopy diagnostic for direct measurements of the local electric field in the edge region of NSTX/NSTX-U: Modeling, Rev. Sci. Instrum. **89** (2018) 10C106.
[24] Hicks W.W., et al., Combined Zeeman and high-frequency Stark effects, with applications to neutral-helium lines useful in plasma diagnostics, Phys. Rev. A **5** (1972) 490.
[25] Kamp A., Himmel G., Determination of rf electric field strengths in deuterium from satellite structure of Balmer lines, Appl. Phys. B **47** (1988) 177.
[26] Martin E.H., et al., A spectroscopic electric field vector imaging diagnostic for electron cyclotron heating systems, Rev. Sci. Instrum. **89** (2018) 10D117.
[27] Martin E.H., Electric field measurements of the capacitively coupled magnetized RF sheath utilizing passive optical emission spectroscopy, Ph.D. thesis, North Carolina State University, 2014.
[28] Martin E.H., et al., Electric field determination in the plasma-antenna boundary of a lower-hybrid wave launcher in Tore Supra through dynamic Stark-effect spectroscopy, Plasma Phys. Control. Fusion **57** (2015) 065011.
[29] Labombard B., KN1D: A 1-D space, 2-D velocity, kinetic transport algorithm for atomic and molecular hydrogen in an ionizing plasma, Massachusetts Institute of Technology, Plasma Science and Fusion Center, RR-01-3.
[30] Wright J.C., Bonoli P.T., Full wave simulations of fast mode conversion and lower hybrid wave propagation in tokamaks, Phys. Plasmas **11** (2004) 2473.
[31] Shiraiwa S., et al., Plasma wave simulation based on a versatile finite element method solver, Phys. Plasmas **17** (2010) 056119.
[32] Meneghini O., et al., Full wave simulation of lower hybrid waves in Maxwellian plasma based on finite element method, Phys. Plasmas **16** (2009) 090701.
[33] Hillairet J., et al., ALOHA: an Advanced Lower Hybrid Antenna coupling code, Nucl. Fusion **50** (2010) 125010.
[34] Lau C., et al., First results of the SOL reflectometer on Alcator C-Mod, Rev. Sci. Instrum. **83** (2012) 10E309.

[35] Hughes J.W., et al., High-resolution edge Thomson scattering measurements on the Alcator C-Mod tokamak, Rev. Sci. Instrum. **72** (2001) 1107.
[36] Stix, T.H., Waves in Plasmas, American Institute of Physics, 1992.
[37] Lau, C., et al., A 3-D synthetic diagnostic of the lower hybrid wave electric field vector in a turbulent plasma in Alcator C-Mod, to be published.
[38] Terry J.L., et al., Spatial structure of scrape-off-layer filaments near the midplane and X-point of Alcator-C-Mod, J. Nucl. Mater. **390** (2009) 339.
[39] Smick N., et al., Transport and drive-driven plasma flow components in the Alcator C-Mod boundary plasma, Nucl. Fusion **53** (2013) 023001.
[40] Zweben S.J. et al., Edge turbulence imaging in the Alcator C-Mod tokamak, Phys. Plasmas **9** (2002) 1981.
[41] Umansky M.V., et al., Simulation of turbulence in the divertor region of tokamak edge plasma, J. Nucl. Mater. **337** (2005) 266.
[42] Bonoli P.T., et al., High field side lower hybrid wave launch for steady state plasma sustainment, Nucl. Fusion **58** (2018) 126032.
[43] Wallace G.M. et al., High field side LHCD in DIII-D: physics demonstration of reactor relevant current drive, EPS 45th Conference on Plasma Physics, July 6th 2018.
[44] Kim J. et al., High field side LHCD launcher study for KSTAR, Fusion Eng. Des., https://doi.org/10.1016/j.fusengdes.2018.12.078.